

# Geophysical Research Letters

## RESEARCH LETTER

10.1029/2020GL087869

### Key Points:

- A multitiered (surface, airborne, mountaintop, and satellite) methane tiered observing system is created for the Los Angeles Basin
- Combining multiple observing system into a single framework allows for increased spatial and temporal sensitivity to methane emissions
- Inverse fluxes from the multitiered system over a large landfill are validated with independent airborne observations

### Supporting Information:

- Supporting Information S1

### Correspondence to:

D. H. Cusworth,  
daniel.cusworth@jpl.nasa.gov

### Citation:

Cusworth, D. H., Duren, R. M., Yadav, V., Thorpe, A. K., Verhulst, K., Sander, S., et al. (2020). Synthesis of methane observations across scales: Strategies for deploying a multitiered observing network. *Geophysical Research Letters*, 47, e2020GL087869. <https://doi.org/10.1029/2020GL087869>

Received 14 JAN 2020

Accepted 13 MAR 2020

Accepted article online 18 MAR 2020

## Synthesis of Methane Observations Across Scales: Strategies for Deploying a Multitiered Observing Network

Daniel H. Cusworth<sup>1</sup> , Riley M. Duren<sup>1,2</sup> , Vineet Yadav<sup>1</sup> , Andrew K. Thorpe<sup>1</sup> , Kristal Verhulst<sup>1</sup> , Stanley Sander<sup>1</sup> , Francesca Hopkins<sup>3</sup> , Talha Rafiq<sup>3</sup> , and Charles E. Miller<sup>1</sup> 

<sup>1</sup>Jet Propulsion Laboratory, California Institute of Technology, Pasadena, CA, USA, <sup>2</sup>University of Arizona, Tucson, AZ, USA, <sup>3</sup>Department of Environmental Sciences, University of California, Riverside, CA, USA

**Abstract** Regional methane emissions monitoring is rapidly expanding with increased coverage of surface, airborne, and satellite instruments. We pilot a multitiered observing system in the Los Angeles Basin. We combine surface methane measurements from the Los Angeles Megacities Carbon Project, mountaintop retrievals from the CLARS-FTS instrument, and space-based  $X_{\text{CH}_4}$  retrievals from the TROPOMI instrument into a single monitoring framework. We simulate these observations using a high-resolution tracer transport model. Using inverse methods, we compare the sensitivity of each observing system component to various emissions sources. Combining multiple observing system into one framework allows for increased spatial and temporal sensitivity to methane emissions. We find a close correspondence between these inverse flux trends and independent airborne AVIRIS-NG methane plume trends over a large landfill in the Los Angeles Basin. These results show that multitiered observing systems can reveal insights about sub-basin scale methane emissions, which can be used to drive decision support.

**Plain Language Summary** Methane is a powerful greenhouse gas. In order to effectively reduce its atmospheric concentrations, we need advanced methane observing strategies to pinpoint large emissions on small spatial scales. In this study, we combine surface, mountaintop, and satellite observations of methane over Los Angeles (called a multitiered observing system) and use these data to infer information about urban methane emissions. We assess how much information each component of the observing system provides to this analytics system. We validate our findings with independent airborne methane fluxes derived from the AVIRIS-NG airborne instrument over a large landfill. Both systems detected large emission reductions that resulted from improved management practices. A multitiered observing and analytics system can potentially provide sub-basin scale decision support for methane mitigation.

## 1. Introduction

Methane is a powerful greenhouse gas with large and highly uncertain natural and anthropogenic sources (Kirschke et al., 2013). Field studies have shown that anthropogenic methane emissions often exhibit fat-tailed distribution, meaning that a small number of point sources constitute a large fraction of the total budget (Duren et al., 2019; Frankenberg et al., 2016; Lyon et al., 2015). Regional and urban scale monitoring of methane has proven successful at detecting large emission anomalies or constraining basin-wide flux estimates (Ware et al., 2019; Yadav et al., 2019). Current and future satellite remote sensing capabilities are ushering in a new era where monitoring of methane point sources may be feasible (Cusworth et al., 2018, 2019; Varon et al., 2018). In this study, we develop a strategy for a multitiered observing system, leveraging multiple independent methane observation methods across a range of spatiotemporal scales to constrain local to regional methane flux estimates and monitor large point sources.

Urban methane studies often rely on multiple observations from a single observing system to constrain emission fluxes. Using a network of in situ atmospheric methane observations in the Los Angeles Basin (Verhulst et al., 2017), Yadav et al. (2019) estimated emission fluxes for 2015–2016 using an atmospheric inversion and found that the results captured changes associated with known events—the Aliso Canyon blowout (Conley et al., 2016), and the closing of the Puente Hills Landfill. Complementing the surface in situ measurements is

the California Laboratory for Atmospheric Remote Sensing (CLARS) Fourier Transform Spectrometer (FTS), located on Mount Wilson 1,700 m above the Los Angeles Basin. The CLARS-FTS scans the basin hourly, mimicking a geostationary satellite, collecting spatially resolved methane slant columns from spectra of reflected sunlight (Fu et al., 2014). Wong et al. (2016) derived a basin-total flux using CO-CH<sub>4</sub> tracer-tracer correlations from CLARS-FTS data and found that methane emissions in the basin varied from 23 to 39 Gg month<sup>-1</sup> during 2011–2015, and He et al. (2019) showed that basin-wide CH<sub>4</sub> fluctuated seasonally with natural gas consumption.

Airborne campaigns have also mapped and quantified methane point source emissions. The AVIRIS-C instrument flew over the Aliso Canyon blowout and was able to detect and constrain its emission characteristics (Thompson et al., 2016). The next generation AVIRIS-NG instrument, with higher spectral resolution and signal-to-noise ratio (SNR), was flown over the Four Corners oil/gas region of New Mexico in April 2015 (Frankenberg et al., 2016) and also across the state of California during 2016 to 2018 (Duren et al., 2019). These studies benefitted from direct imaging of methane plumes with meter-scale spatial resolution. Both the Four Corners and California surveys found that methane emissions follow fat-tailed distributions, with 10% to 20% of point sources constituting 30% to 50+% of the total observed emissions. However, gaps in temporal coverage make it difficult to assess the persistence of high or anomalous methane emitters with airborne monitoring even when sampling such emitters multiple times.

Recent satellite sensors provide much improved spatial and temporal coverage of global methane. The Tropospheric Measuring Instrument (TROPOMI) on Sentinel 5-P (launched October 2017) provides daily 7 × 7 km<sup>2</sup> nadir global coverage of dry air column methane ( $X_{\text{CH}_4}$ ) with uniform sensitivity down to the surface (Hu et al., 2018). The future GeoCARB mission, scheduled for launch in the early 2020s, will provide up to four times per day scanning of a basin at 3 × 3 km<sup>2</sup> nadir resolution (O'Brien et al., 2016). New satellite imaging spectrometers with the potential to detect methane emissions at 30 × 30 m<sup>2</sup> spatial resolution have been launched or will be launched in the near future (Green et al., 2018; Guanter et al., 2015; Loizzo et al., 2018). These instruments have spectral characteristics similar to AVIRIS, and studies have shown that they can potentially detect methane point sources as small as 100 kg hr<sup>-1</sup> (Cusworth et al., 2019). Major drawbacks of satellite monitoring are cloud interference and much lower sensitivity to surface emissions when compared to surface or airborne observations.

Each methane observing configuration (surface, mountaintop, airborne, and spaceborne) presents its own unique strengths and weaknesses. In this study, we combine information from each of these observing systems into a multitiered system to amplify their respective strengths. We focus on the Los Angeles Basin for the study period of January 2017 to September 2018, where ample surface and satellite observations exist. We combine these observations into a regional 3 × 3 km<sup>2</sup> flux inversion and show a specific case of the Sunshine Canyon Landfill, where the multitiered system inversion predicted an emission reduction that was verified with repeated AVIRIS-NG overflights. The results from this study show that a multitiered inverse system provides sub-basin scale information about methane emission characteristics.

## 2. Methane Observing Systems

The spatial coverage of current methane observing systems in the Los Angeles Basin is shown in Figure 1. As part of the Los Angeles Megacities Carbon Project, 14 surface stations in the Southern California Air Basin measure carbon dioxide, methane, and water vapor using wavelength-scanned cavity ring-down spectroscopy instruments (supporting information Figure S1; Verhulst et al., 2017). Site selection was initially based on a theoretical atmospheric transport simulation that specified geolocations necessary to constrain basin-wide carbon dioxide emissions (Kort et al., 2013). For this study, we use eight of the surface sites that are located within the Los Angeles urban domain and that operated continuously during the study period. The CLARS observatory is a mountaintop site located 1,700 m above sea level and has a nearly unobstructed view of the entire Los Angeles Basin (Fu et al., 2014). At CLARS, an FTS instrument views the basin through a pointing system, which allows for continual scanning of designated ground targets daily. The TROPOMI instrument provides 7 × 7 km<sup>2</sup> nadir pixel resolution and daily global coverage of  $X_{\text{CH}_4}$  given sufficiently clear-sky conditions. The AVIRIS-NG instrument was flown over Los Angeles several times between 2016 and 2018 during the California Methane Survey (Duren et al., 2019). The instrument flew at altitudes from 3 to 4 km, providing ground sampling with 3 to 4 m spatial resolution. AVIRIS-NG retrieves methane from

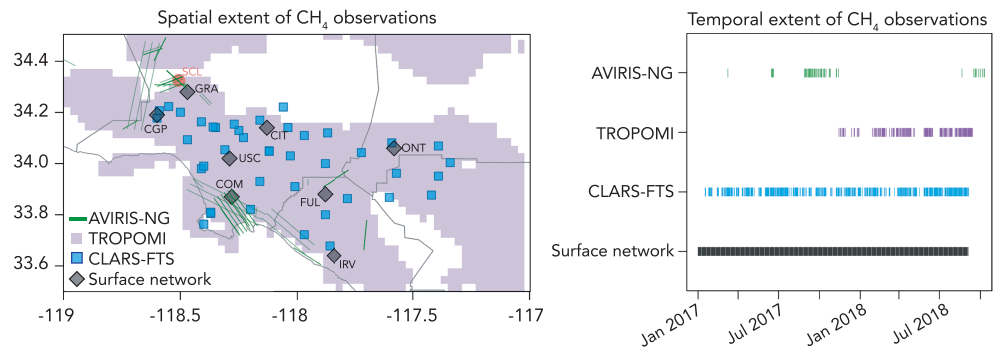


**Figure 1.** Available methane observations during the study period (January 2017 to September 2018). The left panel shows the geolocations of the Los Angeles Megacities Carbon Project surface network sites, CLARS-FTS ground targets, and an envelope showing where TROPOMI provides successful retrievals during the study period. The location of the Sunshine Canyon Landfill (SCL) is also marked on the left panel. The right panel shows the temporal availability of methane observations during the study period. For each day in the study period, a marker is placed on the plot if the given observing system made at least one successful observations within the basin.

the same 2,300 nm absorption band used by TROPOMI, albeit at a much coarser 5 nm spectral resolution. AVIRIS-NG methane mixing ratios (units ppm-m) were retrieved using a linearized match filter approach (Thompson et al., 2016).

Figure 1 shows the temporal coverage of methane observations from each observing system for January 2017 to September 2018. The surface network and CLARS-FTS provide near continual uninterrupted coverage during this period. TROPOMI temporal coverage is limited during the study period due to its late 2017 launch, and its spatial coverage is limited when excessive cloud coverage permeates the basin. AVIRIS-NG campaigns were conducted at discrete intervals under clear-sky conditions, yielding sparse temporal coverage.

### 3. Multitiered Observing and Analytics System

#### 3.1. Forward Model and Observing Sensitivity

Tracer transport models transform an emission state vector  $\mathbf{x}$  (units  $\mu\text{mol m}^{-2} \text{s}^{-1}$ ) to a methane surface or column mole fraction estimate. The Stochastic Time-Inverted Lagrangian Transport (STILT) model is a receptor-oriented particle dispersion model that releases and tracks theoretical particles backwards in time from an observing location and time (Fasoli et al., 2018). The distribution of these particles upwind defines a Jacobian matrix  $\mathbf{H}$  (i.e., influence function or footprint) that is used to relate the emissions to observations:

$$\mathbf{y} = \mathbf{H}\mathbf{x} + \boldsymbol{\epsilon}, \quad (1)$$

where  $\mathbf{y}$  is the observed methane enhancement and  $\boldsymbol{\epsilon}$  is the sum of instrument error, model error, and error in determining the background. Deriving the methane background for each observing system is described in supporting information, section S1 and Figure S2. For TROPOMI, the retrieval algorithms for  $X_{\text{CH}_4}$  are still in active development. We describe our bias correction process in section S1 but expect the type of analysis presented in this study to improve as subsequent iterations of the retrieval are released.

TROPOMI and CLARS-FTS retrievals are sensitive to either the total or slant column of atmospheric methane, so we generate STILT footprints at multiple intervals along their observing paths. The footprints are then pressure weighted and combined using the respective instrument's averaging kernel, which is generally uniform in the troposphere (Butz et al., 2012; Fu et al., 2014). The units for a slant or total column methane retrieval are in dry column mean mixing ratio (ppb).

We use the  $3 \times 3 \text{ km}^2$  High Resolution Rapid Refresh (HRRR) meteorological reanalysis product to drive STILT simulations (Benjamin et al., 2016). Yadav et al. (2019) used higher-resolution meteorology ( $1.3 \times 1.3 \text{ km}^2$ ) from the Weather and Research Forecasting Model (WRF) for Southern California Air Basin methane inversions. The computation of these meteorological fields is expensive and requires

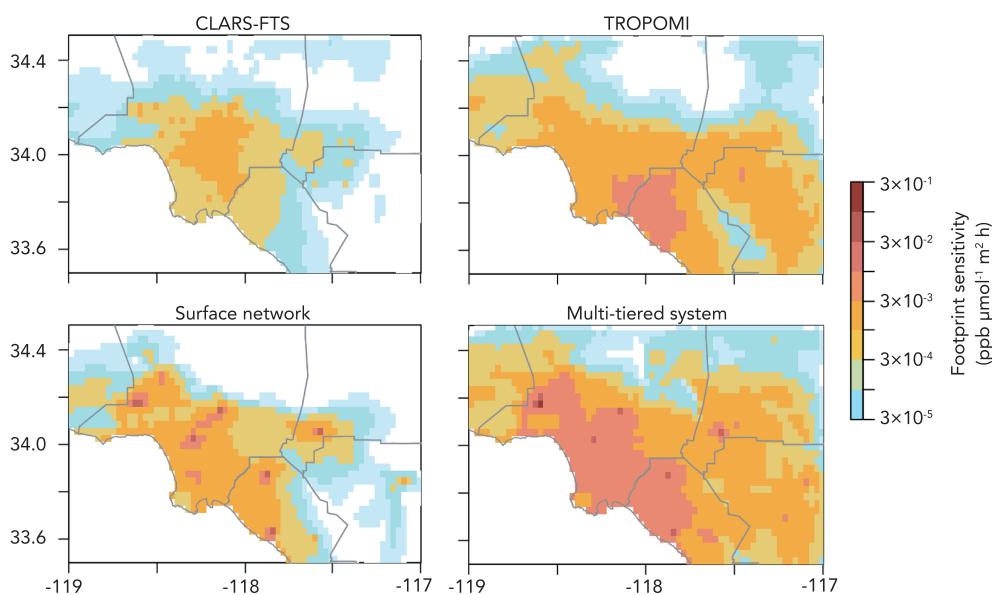


**Figure 2.** Average footprint sensitivity (matrix  $\mathbf{H}$  in equation (1)) for a CLARS-FTS scan of the basin, a single TROPOMI overpass, a single hour of the surface network, and all combined into a multitiered system. Each grid cell value represents the mean contribution that an emission at that location has on a downwind receptor for the given observing system.

considerable resources. Low-latency emissions monitoring is a major goal for multitiered observing system, so we opt instead for HRRR reanalysis.

For the surface network, we generate HRRR-STILT footprints at 4 hr intervals for both day and night. For CLARS-FTS, we generate footprints at 4 hr intervals, but only during daylight hours, when CLARS-FTS is capable of retrieving methane. TROPOMI has a 1:30 PM local time overpass. We generate footprints for clear-sky, successful retrievals. We simulate footprints at  $3 \times 3 \text{ km}^2$  spatial resolution over the basin, which provides a total of 1,810 discrete state vector elements.

The spatial contours of the Jacobian matrix  $\mathbf{H}$  show the extent of observing sensitivity throughout the basin (Figure 2). The TROPOMI  $\mathbf{H}$  matrix covers the largest area of any observing system, as expected. Variability in TROPOMI sensitivity is due to the topography of Los Angeles. Greater sensitivity is seen in regions where the terrain is much flatter. The surface network often has higher sensitivities, especially near each tower. The multitiered system leverages both of these strengths to maximize the basin's observing sensitivity spatial extent and magnitude (Figure S3). TROPOMI's extended spatial coverage gives the system useful sensitivity in the far field, where other monitoring systems lack sensitivity. The surface network provides enhanced sensitivity to emission sources within a 5 to 10 km radius of the towers. CLARS-FTS performance falls in between TROPOMI and the surface network. A single basin-wide survey of CLARS-FTS provides less spatial coverage than TROPOMI and smaller basin sensitivity (Figure S3). However, CLARS-FTS scans the basin three to eight times per day, meaning that over the course of a single day, it provides in sum greater total basin footprint sensitivity than TROPOMI, which is useful in regions that are not well characterized by the surface network. In Figure S4, we sum the total sensitivity of each observing component over the entire study period. Like Figure 2, the maximum sensitivity to emissions comes from the tower network, but TROPOMI still provides greater spatial coverage.

### 3.2. Inverse Model and Error Correlation Parameterization

To infer gridded methane emissions, we build on the inverse framework described in Yadav et al. (2019), with modifications to account for multiple observing systems. Given a set of observations  $\mathbf{y}$  and a Jacobian matrix  $\mathbf{H}$ , we employ an inverse method to derive the optimal estimate  $\hat{\mathbf{x}}$  using the Maximum A Posteriori (MAP) method similar to previous methane inversion studies (e.g., Bergamaschi et al., 2009; Kort et al., 2014; Ware et al., 2019; Wecht et al., 2014; Yadav et al., 2019). Here an objective function  $J(\mathbf{x})$

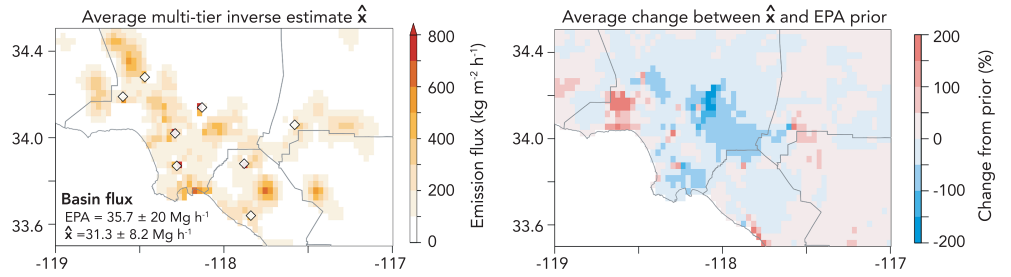


**Figure 3.** Inverse methane emission estimates from the multitiered inversion ( $\hat{\mathbf{x}}$ ). The left panel shows the average  $\hat{\mathbf{x}}$  estimate (in  $\text{kg m}^{-2} \text{hr}^{-1}$ ) over the study period. Overlaid are the locations of the surface network. The right panel shows the average change between  $\hat{\mathbf{x}}$  and the EPA prior emission inventory. Total basin fluxes averaged over the study period are inset. Prior uncertainty is prescribed using the restricted maximum likelihood (section S2), and average posterior uncertainty is calculated by integrating the posterior error covariance matrix  $\hat{\mathbf{S}}$ .

is created to balance model-data mismatch and the deviation from a prior emission field  $\mathbf{x}_A$ , which are both assumed to be distributed normally (Rodgers, 2000):

$$J(\mathbf{x}) = (\mathbf{y} - \mathbf{H}\mathbf{x})^T \mathbf{R}^{-1} (\mathbf{y} - \mathbf{H}\mathbf{x}) + (\mathbf{x} - \mathbf{x}_A)^T \mathbf{S}^{-1} (\mathbf{x} - \mathbf{x}_A), \quad (2)$$

where  $\mathbf{R}$  is the observational error covariance matrix and  $\mathbf{S}$  is the prior error covariance matrix. These matrices weight the influence of model-data mismatch and deviation from the prior on the optimal solution  $\hat{\mathbf{x}}$ , respectively. The optimal solution  $\hat{\mathbf{x}}$  and associated posterior error covariance matrix  $\hat{\mathbf{S}}$  are found by minimizing  $J(\mathbf{x})$  and take the following form:

$$\hat{\mathbf{x}} = \mathbf{x}_A + \mathbf{S}\mathbf{H}^T (\mathbf{H}\mathbf{S}\mathbf{H}^T + \mathbf{R})^{-1} (\mathbf{y} - \mathbf{H}\mathbf{x}), \quad (3)$$

$$\hat{\mathbf{S}} = (\mathbf{H}^T \mathbf{R}^{-1} \mathbf{H} + \mathbf{S}^{-1})^{-1}. \quad (4)$$

The information content provided from the inversion can be quantified by looking at the averaging kernel matrix  $\mathbf{A}$  (Jacob et al., 2016):

$$\mathbf{A} = \frac{\partial \hat{\mathbf{x}}}{\partial \mathbf{x}} = \mathbf{I}_N - \hat{\mathbf{S}}\mathbf{S}^{-1}. \quad (5)$$

The averaging kernel represents how much the posterior solution was influenced by the true emission state. The trace of the averaging kernel, also called degrees of freedom for signal (DOFS), describes how many pieces of independent information the observing system provided on the emission field (Jacob et al., 2016).

We use restricted maximum likelihood to generate the diagonal terms of the  $\mathbf{R}$  and  $\mathbf{S}$  matrices in equation (2), as has been done in previous regional inverse studies (Michalak et al., 2005; Yadav et al., 2019). We include additional off-diagonal terms in both  $\mathbf{R}$  and  $\mathbf{S}$  to account for correlation between model transport error, correlation between observations from different observing system components, and correlation between prior state vector elements following the approaches of previous regional inverse modeling studies (section S2; Cusworth et al., 2018; Turner et al., 2018).

We perform separate inversions for every 2 week interval over the course of the study period, provided that observations from each observing system are available. We use the 2012 EPA gridded  $0.1^\circ \times 0.1^\circ$  methane inventory (Maasackers et al., 2016) as the prior emission field. Prior uncertainty scale factors (section S2) are recomputed for each 2 week interval. Through the application of equations (S1)–(S5), the median prior uncertainty scale factor for the multitiered system was estimated to be 56% of the EPA prior emission rate.

## 4. Results

### 4.1. Inverse Flux Estimates Over the Los Angeles Basin

Figure 3 shows the average optimal methane emission estimate  $\hat{\mathbf{x}}$  during the study period for the multitiered system in absolute flux units ( $\text{kg m}^{-2} \text{s}^{-1}$ ) and relative to the EPA prior (% change). We display results in %

change to highlight regions that may anomalously differ from the prior. A few spatial inconsistencies between the prior inventory and  $\hat{\mathbf{x}}$  emerge in Figure 3. For example, large hot spots appear on the western edge of Los Angeles County (34.2°N, -118.6°E), near Mid-City/Downtown Los Angeles (34.0°N, -118.3°E), and along the Orange County Coast (33.6°N, -117.8°E), which are most likely due to unaccounted industrial and oil/gas activity in the prior inventory. Another hot spot appears near the Sunshine Canyon Landfill (SCL in Figure 1; 34.3°N, -118.5°E; described in greater detail in section 4.2). A large reduction in emissions from  $\hat{\mathbf{x}}$  compared to the prior appears around 34.2°N, -118.0°E. This is a mountainous region of Los Angeles, so although the relative change in emissions is large, the absolute flux deviation from the prior is small.

The prior and optimized solution  $\hat{\mathbf{x}}$  mostly agree on basin-total emission rates, as the multitiered inversion predicts slightly lower basin-total emissions ( $31.3 \pm 8.2 \text{ Mg hr}^{-1}$ ) than the EPA inventory ( $35.7 \pm 20 \text{ Mg hr}^{-1}$ ). The basin-total emission rate is smaller, but within the uncertainties of emissions reported in previous studies (e.g.,  $38.10 \pm 10 \text{ Mg hr}^{-1}$  for 2015 to 2016 in Yadav et al., 2019). However, the present study uses a different spatial domain, meteorological fields, prior inventory, and time period. Both the present study and Yadav et al. (2019) find the basin-total inverse estimate to be slightly lower than the respectively chosen prior inventory. The uncertainty in the inverse emission rate is derived by integrating the information from  $\hat{\mathbf{S}}$ . On the basin scale, the inversion reduced emission uncertainty by 60%.

The first term on the right-hand side of equation (2) minimizes model-data mismatch, so to assess the observational constraints of the inversion, we compare the root-mean-square error (RMSE) between observations and the forward model driven by either the prior or posterior emissions. We find that on average during the study period, the RMSE between the posterior model and observations was reduced by 38.1% for TROPOMI, and 27.4% for CLARS-FTS, and 36.5% for the surface network, relative to the RMSE for the prior model. The 60% uncertainty reduction from  $\hat{\mathbf{S}}$  and the 27.4–36.5% RMSE error reduction show that the multitiered observing system provides robust constraints to basin scale emissions.

We follow equation (5) and compute the average DOFS for each component of the multitiered system during the study period. The DOFS for the multitiered system is 105, meaning that the observing system is able to constrain on average 105 distinct emission elements during each 2 week interval. For TROPOMI, CLARS-FTS, and the surface network, the DOFS are 59, 23, and 85, respectively, meaning that the tower network provides the strongest constraint on  $\hat{\mathbf{x}}$ . However, TROPOMI and CLARS provide nontrivial information as the DOFS increases by 20 when the full multitiered system is implemented. As seen in Figure 2, much of this additional information is a result of the broader spatial coverage provided by TROPOMI. The significant number of DOFS means that the multitiered system may be able to constrain sub-basin scale emissions in regions that are well observed and have large emission sources. We explore a specific example of sub-basin scale analysis in section 4.2.

We perform inversions separately for each component of the observing system to test for spatial coherence in  $\hat{\mathbf{x}}$ . Figure S5 shows the inverse estimate for each component of the observing system. Each system independently infers a basin-total flux rate ( $30.5\text{--}33.7 \text{ Mg hr}^{-1}$ ) that agrees with one another within their uncertainty bounds. Each component spatially agrees in sign with many of the regions shown in Figure 3, specifically higher than reported EPA emissions over the western edge of Los Angeles, and lower than reported emissions over the San Gabriel Mountains. Both TROPOMI and CLARS-FTS generally infer lower Los Angeles metropolitan emissions than the tower network, which is likely due to the lower sensitivity of column and slant to small and diffuse methane sources and temporal variability in emissions. TROPOMI also predicts higher emissions in Riverside County (33.9°N, -117.5°E) and Ventura County (34.2°N, -119.0°E). The northwestern border of Riverside and San Bernardino counties contain many dairies, and Ventura County contains many oil and gas fields (Carranza et al., 2018), which may be the cause of these higher predicted emissions. The enhancement seen from the TROPOMI-alone inversion (Figure S5) is an important result as it shows that the limited spatial sensitivity of the tower network and CLARS-FTS (Figure 2) may omit significant emissions on the outskirts of the urban domain.

#### 4.2. Sub-Basin Scale Emissions and Validation With Airborne Observations

The significant DOFS inferred by the multitiered system in section 4.1 suggest that sub-basin scale analyses of methane emissions are possible. We assess the north region of Los Angeles County around the Aliso

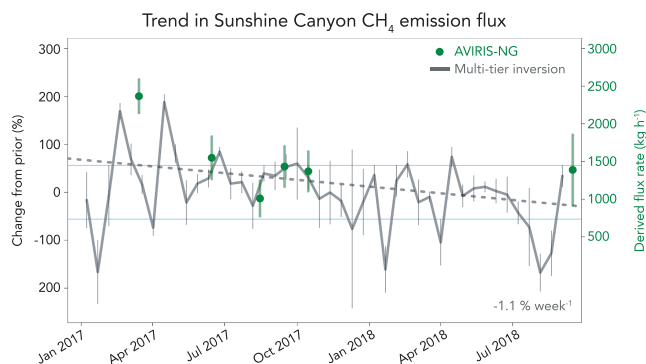


**Figure 4.** Trends in emission estimates at the Sunshine Canyon Landfill (SCL in Figure 1). In the top panel, the gray line represents the trend in the  $3 \times 3 \text{ km}^2$  grid cell of the multitiered  $\hat{\mathbf{x}}$  that contained the SCL. Error bars represent the associated posterior uncertainty from the diagonal of  $\hat{\mathbf{S}}$  with added correlated off-diagonal error. The dashed gray line is the trend in  $\hat{\mathbf{x}}$ , which is significant at  $p < 0.05$  and weighted using the posterior error covariance. The green dots represent the monthly mean AVIRIS-NG derived emission flux rates for SCL. Error bars represent the spread in derived flux rates when the hyper-parameters used to determine plume enhancements and the wind speeds are varied (section S3). Blue lines represent the average prior uncertainty prescribed in the inversion setup.

Canyon oil/gas field and SCL where many independent airborne methane flux measurements were taken using the AVIRIS-NG instrument as part of the California Methane Survey (Duren et al., 2019; supporting information, section S3). These independent observations allow for validation of the spatial variance of the multitiered inverse flux estimates. We detected a hot spot around this area consistent with large observed methane variability at the Granada Hills network site (GRA in Figure 1; 5 km southeast of SCL; Verhulst et al., 2017), and EPA estimates 14.5 million kg  $\text{CH}_4$  were reportedly emitted at SCL in 2017 (EPA, 2020). Since the inversion is unable to differentiate between co-located sources in the same 3 km grid cell, additional observations are required for source attribution. AVIRIS-NG flew over Aliso Canyon and SCL multiple times during the California Methane Survey. The Aliso Canyon blowout was resealed in February 2016, and the residual emissions observed by AVIRIS-NG at the site were insufficient to account for the methane enhancement determined from the inversion in 2017 to 2018. However, AVIRIS-NG observed large methane enhancements over the intermediate cover slopes at SCL at the onset of the campaign. Contact was made with the landfill local enforcement agency. Antecedent poor management practices led to persistent methane blowouts along intermediate cover slopes. At the time of the first AVIRIS-NG overpass, SCL was in early stages of planned infrastructure remediation that had been prompted by a high volume of odor complaints

from the surrounding community (Cusworth et al., 2020).

Figure 4 displays the time series of methane emissions from the  $3 \times 3 \text{ km}^2$  grid cell of  $\hat{\mathbf{x}}$  that contains SCL determined from the multitiered inversion. Error bars represent the associated posterior uncertainty from the diagonal of  $\hat{\mathbf{S}}$  with added correlated off-diagonal error. Superimposed on this time series are the AVIRIS-NG emission rates derived from individual flight days. AVIRIS-NG maps plumes on specific sections of the landfill, and the multitiered inversion is sensitive to the larger  $9 \text{ km}^2$  grid cell as well as any correlated influence from emission elements in the surrounding residential and oil/gas sectors. However, if AVIRIS-NG plumes are the dominant contributors to methane concentrations in the local area, the variability and trend should be captured in the multitiered inversion. This is precisely what is seen in Figure 4, where the inverse flux estimate fluctuates dramatically from January to May 2017, which is consistent with the large  $2,300 \text{ kg hr}^{-1}$  flux rate derived from AVIRIS-NG in March 2017. Starting around June 2017, flux estimates from the inversion and AVIRIS-NG begin to decrease. We fit a least squares regression model weighted by the posterior error covariance to the SCL inverse emission estimate. We find a significant 1.1% per week decrease in emissions ( $p < 0.05$ ). Both the inversion and AVIRIS-NG derived trends are consistent with the timing of facility scale improvements. The inversion also reduced the uncertainty on the gridded emission estimate at SCL on average by 33% relative to the prior uncertainty.

The close correspondence in independent SCL emission estimates from  $\hat{\mathbf{x}}$  and AVIRIS-NG highlight the ability of the multitiered system to provide sub-basin scale actionable information. Though AVIRIS-NG flights were completed prior to this study, these results show that multitiered observing and analytics system can be employed to target sub-basin scale regions of interest. From there, additional mobile, airborne, or future satellite remote sensing can be deployed to provide actionable process-level emission understanding.

## 5. Summary

We developed a methane synthesis and emission estimation framework in the Los Angeles urban domain. We combined surface (Los Angeles Megacities Carbon Project), mountaintop (CLARS-FTS), and satellite (TROPOMI) methane observations into a single multitiered observing framework for January 2017 to September 2018, with additional information on specific emitters from airborne (AVIRIS-NG) observations. We simulated surface, CLARS-FTS, and TROPOMI observations using the HRRR-STILT tracer transport model and derived optimal emission flux rates for each 2 week period during the study period. We found that

a multitiered synthesis was able to detect reduction in methane emissions at Sunshine Canyon Landfill, which corresponds closely to infrastructure changes undertaken at the landfill.

We find that in the Los Angeles Basin, the majority of the information for the multitiered system comes from the tower network. However, by looking at the degrees of freedom for signal for each component of the observing system, we see that TROPOMI and CLARS-FTS provide complementary information, especially on the margins of the urban domain that are not well covered by the tower network.

Multitiered observing of methane has the potential for advanced emissions monitoring. Measuring carbon emissions from megacities is an urgent matter. Deploying additional atmospheric observations of methane from the surface to space can be transformative to emission monitoring, as long as they combined in an efficient and efficacious fashion. The framework we present in this study is successful for Los Angeles and can be extended to other regions where methane monitoring is a priority.

## 6. Data Availability Statement

Tower data from the Los Angeles Megacities Carbon Project and slant column retrievals from CLARS-FTS are available for download (at <https://megacities.jpl.nasa.gov/portal/>). TROPOMI data are available online (at <https://s5phub.copernicus.eu/>). AVIRIS-NG radiances are available online (at [https://avirisng.jpl.nasa.gov/alt\\_locator/](https://avirisng.jpl.nasa.gov/alt_locator/)). The STILT model with installation instructions is available for download (at <https://uataq.github.io/stilt/>). VISTA-LA data are available for download (at [https://daac.ornl.gov/cgi-bin/dviewer.pl?ds\\_id=1525](https://daac.ornl.gov/cgi-bin/dviewer.pl?ds_id=1525)).

### Acknowledgments

This work was supported in part by NASA's Carbon Monitoring System (CMS) Prototype Methane Monitoring System for California. Data from the California Methane Survey was supported by NASA's Earth Science Division, the California Air Resources Board (ARB) under ARB-NASA Agreement 15RD028, Space Act Agreement 82-19863, and the California Energy Commission under CEC-500-15-004. A portion of this work was performed at the Jet Propulsion Laboratory, California Institute of Technology, under contract with NASA. Copyright California Institute of Technology, 2019. All Rights Reserved. Government funding acknowledged.

### References

- Benjamin, S. G., Weygandt, S. S., Brown, J. M., Hu, M., Alexander, C. R., Smirnova, T. G., et al. (2016). A North American hourly assimilation and model forecast cycle: The Rapid Refresh. *Monthly Weather Review*, *144*, 1669–1694. <https://doi.org/10.1175/MWR-D-15-0242.1>
- Bergamaschi, P., Frankenberg, C., Meirink, J. F., Krol, M., Villani, M. G., Houweling, S., et al. (2009). Inverse modeling of global and regional methane emissions using SCIAMACHY satellite retrievals. *Journal of Geophysical Research*, *114*, D22301. <https://doi.org/10.1029/2009JD012287>
- Butz, A., Galli, A., Hasekamp, O., Landgraf, J., Tol, P., & Aben, I. (2012). TROPOMI aboard Sentinel-5 Precursor: Prospective performance of methane retrievals for aerosol and cirrus loaded atmospheres. *Remote Sensing of Environment*, *120*, 267–276. <https://doi.org/10.1016/j.rse.2011.05.030>, URL, <http://www.sciencedirect.com/science/article/pii/S003442571200082X>, the Sentinel Missions - New Opportunities for Science
- Carranza, V., Rafiq, T., Frausto-Vicencio, I., Hopkins, F. M., Verhulst, K. R., Rao, P., et al. (2018). Vista-LA: Mapping methane-emitting infrastructure in the Los Angeles megacity. *Earth System Science Data*, *10*, 653–676. <https://doi.org/10.5194/essd-10-653-2018>
- Conley, S., Franco, G., Faloona, I., Blake, D. R., Peischl, J., & Ryerson, T. B. (2016). Methane emissions from the 2015 Aliso Canyon blowout in Los Angeles, CA. *Science*, *351*(6279), 1317–1320.
- Cusworth, D. H., Duren, R., Thorpe, A. K., Tseng, E., Thompson, D., Guha, A., et al. (2020). Using remote sensing to detect, validate, and quantify methane emissions from California solid waste operations. *Environmental Research Letters*. <https://doi.org/10.1088/1748-9326/ab7b99>
- Cusworth, D. H., Jacob, D. J., Sheng, J.-X., Benmergui, J., Turner, A. J., Brandman, J., et al. (2018). Detecting high-emitting methane sources in oil/gas fields using satellite observations. *Atmospheric Chemistry and Physics*, *18*, 16,885–16,896. <https://doi.org/10.5194/acp-18-16885-2018>
- Cusworth, D. H., Jacob, D. J., Varon, D. J., Chan Miller, C., Liu, X., Chance, K., et al. (2019). Potential of next-generation imaging spectrometers to detect and quantify methane point sources from space. *Atmospheric Measurement Techniques*, *12*, 5655–5668. <https://doi.org/10.5194/amt-12-5655-2019>
- Duren, R. M., Thorpe, A. K., Foster, K. T., Rafiq, T., Hopkins, F. M., Yadav, V., et al. (2019). California's methane super-emitters. *Nature*, *575*(7781), 180–184. <https://doi.org/10.1038/s41586-019-1720-3>
- EPA (2020). Greenhouse gases from large facilities, facility level information on greenhouse gases tool. <https://ghgdata.epa.gov/ghgp/main.do>. Last accessed 20 February 2020.
- Fasoli, B., Lin, J. C., Bowling, D. R., Mitchell, L., & Mendoza, D. (2018). Simulating atmospheric tracer concentrations for spatially distributed receptors: Updates to the Stochastic Time-Inverted Lagrangian Transport model's R interface (STILT-R version 2). *Geoscientific Model Development*, *11*, 2813–2824. <https://doi.org/10.5194/gmd-11-2813-2018>
- Frankenberg, C., Thorpe, A. K., Thompson, D. R., Hulley, G., Kort, E. A., Vance, N., et al. (2016). Airborne methane remote measurements reveal heavy-tail flux distribution in Four Corners region. *Proceedings of the National Academy of Sciences*, *113*, 9734–9739. <https://doi.org/10.1073/pnas.1605617113>
- Fu, D., Pongetti, T. J., Blavier, J.-F. L., Crawford, T. J., Manatt, K. S., Toon, G. C., et al. (2014). Near-infrared remote sensing of Los Angeles trace gas distributions from a mountaintop site. *Atmospheric Measurement Techniques*, *7*, 713–729. <https://doi.org/10.5194/amt-7-713-2014>
- Green, R., Mahowald, N., Clark, R., Ehlmann, B., Ginoux, P., Kalashnikova, O., et al. (2018). NASA's Earth Surface Mineral Dust Source Investigation. In AGU Fall Meeting Abstracts, 2018.
- Guanter, L., Kaufmann, H., Segl, K., Foerster, S., Rogass, C., Chabrillat, S., et al. (2015). The EnMAP spaceborne imaging spectroscopy mission for Earth observation. *Remote Sensing*, *7*, 8830–8857. <https://doi.org/10.3390/rs70708830>

- He, L., Zeng, Z. C., Pongetti, T. J., Wong, C., Liang, J., Gurney, K. R., et al. (2019). Atmospheric methane emissions correlate with natural gas consumption from residential and commercial sectors in Los Angeles. *Geophysical Research Letters*, *46*, 8563–8571. <https://doi.org/10.1029/2019GL083400>
- Hu, H., Landgraf, J., Detmers, R., Borsdorff, T., Aan de Brugh, J., Aben, I., et al. (2018). Toward global mapping of methane with TROPOMI: First results and intersatellite comparison to GOSAT. *Geophysical Research Letters*, *45*, 3682–3689. <https://doi.org/10.1002/2018GL077259>
- Jacob, D. J., Turner, A. J., Maasakkers, J. D., Sheng, J., Sun, K., Liu, X., et al. (2016). Satellite observations of atmospheric methane and their value for quantifying methane emissions. *Atmospheric Chemistry and Physics*, *16*, 14,371–14,396. <https://doi.org/10.5194/acp-16-14371-2016>
- Kirschke, S., Bousquet, P., Ciais, P., Saunoy, M., Canadell, J., Dlugokencky, E., et al. (2013). Three decades of global methane sources and sinks. *Nature Geoscience*, *6*(10), 813–823.
- Kort, E. A., Angevine, W. M., Duren, R., & Miller, C. E. (2013). Surface observations for monitoring urban fossil fuel CO<sub>2</sub> emissions: Minimum site location requirements for the Los Angeles megacity. *Journal of Geophysical Research: Atmospheres*, *118*, 1577–1584. <https://doi.org/10.1002/jgrd.50135>
- Kort, E. A., Frankenberg, C., Costigan, K. R., Lindenmaier, R., Dubey, M. K., & Wunch, D. (2014). Four corners: The largest US methane anomaly viewed from space. *Geophysical Research Letters*, *41*, 6898–6903. <https://doi.org/10.1002/2014GL061503>
- Lyon, D., Zavala-Araiza, D., Alvarez, R., Harriss, R., Palacios, V., Lan, X., et al. (2015). Constructing a Spatially Resolved Methane Emission Inventory for the Barnett Shale Region. *Environmental Science & Technology*, *49*(13), 8147–8157. <https://doi.org/10.1021/es506359c>
- Loizzo, R., Guarini, R., Longo, F., Scopa, T., Formaro, R., Facchinetti, C., & Varacalli, G. (2018). Prisma: the Italian hyperspectral mission. In *IGARSS 2018-2018 IEEE International Geoscience and Remote Sensing Symposium, Valencia* (pp. 175–178). <https://doi.org/10.1109/igarss.2018.8518512>
- Maasakkers, J. D., Jacob, D. J., Sulprizio, M. P., Turner, A. J., Weitz, M., Wirth, T., et al. (2016). Gridded national inventory of US methane emissions. *Environmental Science & Technology*, *50*(23), 13,123–13,133. <https://doi.org/10.1021/acs.est.6b02878>
- Michalak, A. M., Hirsch, A., Bruhwiler, L., Gurney, K. R., Peters, W., & Tans, P. P. (2005). Maximum likelihood estimation of covariance parameters for Bayesian atmospheric trace gas surface flux inversions. *Journal of Geophysical Research*, *110*, D24107. <https://doi.org/10.1029/2005JD005970>
- O'Brien, D. M., Polonsky, I. N., Utembe, S. R., & Rayner, P. J. (2016). Potential of a geostationary geoCARB mission to estimate surface emissions of CO<sub>2</sub>, CH<sub>4</sub> and CO in a polluted urban environment: case study Shanghai. *Atmospheric Measurement Techniques*, *9*, 4633–4654. <https://doi.org/10.5194/amt-9-4633-2016>
- Rodgers, C. D. (2000). *Inverse methods for atmospheric sounding: Theory and practice* (Vol. 2). Singapore: World Scientific.
- Thompson, D. R., Thorpe, A. K., Frankenberg, C., Green, R. O., Duren, R., Guanter, L., et al. (2016). Space-based remote imaging spectroscopy of the Aliso Canyon methane superemitter. *Geophysical Research Letters*, *43*, 6571–6578. <https://doi.org/10.1002/2016GL069079>
- Turner, A. J., Jacob, D. J., Benmergui, J., Brandman, J., White, L., & Randles, C. A. (2018). Assessing the capability of different satellite observing configurations to resolve the distribution of methane emissions at kilometer scales. *Atmospheric Chemistry and Physics*, *18*, 8265–8278. <https://doi.org/10.5194/acp-18-8265-2018>
- Varon, D. J., Jacob, D. J., McKeever, J., Jarvis, D., Durak, B. O. A., Xia, Y., & Huang, Y. (2018). Quantifying methane point sources from fine-scale satellite observations of atmospheric methane plumes. *Atmospheric Measurement Techniques*, *11*, 5673–5686. <https://doi.org/10.5194/amt-11-5673-2018>
- Verhulst, K. R., Karion, A., Kim, J., Salameh, P. K., Keeling, R. F., Newman, S., et al. (2017). Carbon dioxide and methane measurements from the Los Angeles Megacity Carbon Project—Part 1: Calibration, urban enhancements, and uncertainty estimates. *Atmospheric Chemistry and Physics*, *17*, 8313–8341. <https://doi.org/10.5194/acp-17-8313-2017>
- Ware, J., Kort, E. A., Duren, R., Mueller, K. L., Verhulst, K., & Yadav, V. (2019). Detecting urban emissions changes and events with a near-real-time-capable inversion system. *Journal of Geophysical Research: Atmospheres*, *124*, 5117–5130. <https://doi.org/10.1029/2018JD029224>
- Wecht, K. J., Jacob, D. J., Sulprizio, M. P., Santoni, G. W., Wofsy, S. C., Parker, R., et al. (2014). Spatially resolving methane emissions in California: Constraints from the CalNex aircraft campaign and from present (GOSAT, TES) and future (TROPOMI, geostationary) satellite observations. *Atmospheric Chemistry and Physics*, *14*, 8173–8184. <https://doi.org/10.5194/acp-14-8173-2014>
- Wong, C. K., Pongetti, T. J., Oda, T., Rao, P., Gurney, K. R., Newman, S., et al. (2016). Monthly trends of methane emissions in Los Angeles from 2011 to 2015 inferred by CLARS-FTS observations. *Atmospheric Chemistry and Physics*, *16*, 13,121–13,130. <https://doi.org/10.5194/acp-16-13121-2016>
- Yadav, V., Duren, R., Mueller, K., Verhulst, K. R., Nehrkorn, T., Kim, J., et al. (2019). Spatio-temporally resolved methane fluxes from the Los Angeles Megacity. *Journal of Geophysical Research: Atmospheres*, *124*, 5131–5148. <https://doi.org/10.1029/2018JD030062>